CrossMark

Synchrotron Cutoff in Ultraluminous X-Ray Sources

Tanuman Ghosh[iD], Shiv Sethi, and Vikram Rana
Astronomy and Astrophysics, Raman Research Institute, C.V. Raman Avenue, Sadashivanagar, Bangalore 560080, India; tanuman@rri.res.in

Abstract

The origin of spectral curvature at energies $E \simeq 10$ keV in ultraluminous X-ray sources (ULXs) is not well understood. In this paper, we propose a novel mechanism based on synchrotron radiation to explain this cutoff. We show that relativistic plasma can give rise to the observed spectral curvature for neutron star magnetic fields due to the variation in the latitude of synchrotron radiation. We analyze the NuSTAR data of two bright pulsar ULXs, NGC 5907 ULX1 and NGC 7793 P13, and provide estimates of the physical parameters of these sources. We fit the data for synchrotron emission at various latitudes and show that the spectral cutoff in these cases can be explained for a large range of acceptable physical parameters, e.g., a semirelativistic plasma with $\gamma \simeq 20$ for high latitudes or a highly relativistic plasma ($\gamma \simeq 10^5$) for emission close to the electron's orbital plane in a typical magnetic field of $B \simeq 10^{12}$ G. We also discuss how such an emission mechanism can be distinguished from other proposed models. A corollary to our study is that most ULXs might be neutron stars as they display such a spectral cutoff.

Unified Astronomy Thesaurus concepts: Radiative processes (2055); Neutron stars (1108); Ultraluminous x-ray sources (2164); High energy astrophysics (739)

1. Introduction

Ultraluminous X-ray sources (ULXs) are some of the brightest known X-ray sources ($L_x > 10^{39}$ erg s^{-1}). Their luminosities exceed the classical Eddington limit of a 10 $M_\odot$ black hole (see Kaaret et al. 2017 for a recent review). In addition, many ULXs display a unique spectral curvature at energies $\simeq 10$ keV, as shown by broadband X-ray data (e.g., Bachetti et al. 2013; Walton et al. 2013). This spectral feature is one of the distinctive characteristics of ULXs compared to the hard state of Galactic X-ray binaries (XRBs) and active galactic nuclei (AGNs). The discovery of a neutron star ULX (Bachetti et al. 2014) changed the perception of these sources, and a foremost conjecture is that a large fraction of the ULX population are neutron stars (e.g., King & Lasota 2016, 2020; King et al. 2017). Many theoretical models have been studied to explain emission mechanisms that generate such high luminosity from neutron stars (e.g., Mushtukov et al. 2015, 2017, 2018, 2019). The origin of spectral cutoff, however, has no compelling theoretical model. Recent observational studies provide phenomenological models that invoke physical scenarios like Compton scattering in the coronal region in low magnetic sources like black holes or Comptonization in the accretion column in highly magnetized neutron stars (see, e.g., Walton et al. 2018a, 2020; West et al. 2018). In this paper, we propose an alternative model based on synchrotron radiation from different latitudes to explain the observed spectral cutoff. We explore the possible physical scenarios of this phenomenon in the context of ULXs and estimate physical parameters related to both the luminosity and the spectral cutoff in ULXs.

Synchrotron radiation is one of the most prevalent radiative processes in astrophysics (Rybicki & Lightman 1979). While the nonrelativistic synchrotron radiation, the cyclotron radiation, provides a discrete spectrum, the emission by relativistic particles yields near-continuum spectrum owing to the higher harmonics contributing more predominantly to the observed spectrum (see Landau & Lifshitz 1975; Rybicki & Lightman 1979 for a review). The astrophysical implications of synchrotron radiation are well studied in multiple wavelengths, including soft to hard X-rays (e.g., Heinz 2004; Maccarone 2005; Markoff et al. 2005; Longair 2011; Kisaka & Tanaka 2017a, 2017b; Riegler 1970). In this paper, we explore the impact of high-latitude, optically thin, classical synchrotron emission on the spectrum of the radiation for a range of speeds encompassing a broad range from semirelativistic to ultrarelativistic electrons.

In the next section, we briefly review the physics of synchrotron radiation relevant to our work. We also provide approximate analytical expressions that allow one to study the emission from semirelativistic to highly relativistic electrons for a range of latitudes. In Section 3, we provide details of the data we use and its preprocessing. The main results are presented in Section 4. In Section 5, we summarize our findings and discuss how our proposed method can be distinguished from other models.

2. Synchrotron Radiation: Semirelativistic to Ultrarelativistic Transition

We assume a geometric construct in which the incoherent synchrotron radiation originates close to the surface of a neutron star. As the length scale of magnetic fields is much larger than the curvature of the gravitating body, we can assume that the magnetic field lines are straight on scales from which the observed synchrotron emission occurs. Without loss of generality, we assume that the magnetic field is in the z-direction of Cartesian geometry and the charged particles move in a circular motion around the uniform magnetic field lines in the xy plane.

The angular distribution of the radiated power in the nth harmonic (or an angular frequency of observation, ω) for a

single electron (ergs per second) per unit solid angle ($d\Omega$) can be expressed as (Landau & Lifshitz 1975):

$$dI_n = \frac{e^2\omega^2}{2\pi c}[\tan^2\theta J_n^2(n\beta\cos\theta) + \beta^2 J_n'^2(n\beta\cos\theta)]d\Omega. \quad (1)$$

Here $\beta = v/c$, B is the magnetic field strength, and θ is the angle between radiated emission and the particle's orbital plane. $J_n(x)$ is the Bessel function, and $J_n'(x)$ is its derivative. The integer n denotes the discrete energy levels of the electron's energy with $\omega = n\omega_B$. $\omega_B = eB/\gamma m_e c$, and $\gamma = 1/\sqrt{1 - \beta^2}$ is the relativistic boost.

The aim of our study is to analyze the emission from both semirelativistic and ultrarelativistic plasmas. Equation (1) allows for the transition from cyclotron to synchrotron radiation. If the argument of the Bessel functions is small, $\beta \ll 1$, the emission is dominated by low multipoles, $n \simeq 1$ (cyclotron radiation with most of the radiation occurring at $\omega \simeq \omega_B$). As the argument of Bessel functions approaches unity, the contribution of higher multipoles increases. In the ultrarelativistic case with $\theta \simeq 0$ (emission close to the plane of rotation), the emission is dominated by multipoles $n \lesssim \gamma^3$, with an exponential cutoff at large frequencies. For $\gamma \gg 1$, the spectral gap between successive multipoles is $\Delta\omega = \omega_B \ll \omega$, and the emission spectrum is near-continuum (synchrotron radiation). We discuss the case of nonzero θ below.

Equation (1) gives the synchrotron spectrum for a single electron of energy $E = m_e c^2 \gamma$. We consider a range of electron energies and model the electron energy distribution using an exponential cutoff power law $f(\gamma) = N\gamma^{-p} \exp(-\gamma/\gamma_{max})$ in the range γ_{min} and γ_{max} (e.g., Reynolds & Keohane 1999). N gives the overall normalization. For our work, we treat γ_{min} as a free parameter, and $\gamma_{max} = 1000\gamma_{min}$. We use the energy spectral index $p = 2.2$, which is consistent with the shock acceleration mechanism (e.g., Allen et al. 2001). For this case, if γ_{max} is larger than γ_{min} by more than a few factors of 10, its impact on our results is found to be negligible. The factors needed for conversion to flux units for comparison with the data are absorbed in the definition of N: $N = \rho_N V/D^2$, where ρ_N is the number density of relativistic electrons, V is the volume of the emitting region, and D is the luminosity distance to the source.

As noted above, Equation (1) allows one to analyze the transition from cyclotron to synchrotron radiation. For large γ, the emission is dominated by large n and is restricted to an angle $\theta \simeq 1/\gamma$ centered on the plane of the orbit. For intermediate γ or semirelativistic electrons ($\gamma \lesssim 10$), it is possible to have substantial emissions from higher latitudes. In this paper, we explore the possibility that the observed radiation could emanate from high latitudes with respect to the plane of the orbit. In this case, $\beta' = \beta\cos\theta$ acts as the effective velocity parameter in Equation (1) and determines the frequency at which the synchrotron spectrum begins to fall exponentially. In Figure 1, we show synchrotron spectra for different values of θ. As expected, for fixed β and B, the spectral cutoff shifts to smaller harmonics n for larger θ.

Figure 1 is based on the numerical evaluation of Bessel functions in Equation (1). One can gain more direct insight into the relevant physics with analytic approximations. In the literature, such analytic expressions have been computed for angle-averaged emission for $\beta \simeq 1$ (e.g., Schwinger et al. 1998). However, such approximations are not valid here as the relevant parameter for us is $\beta\cos\theta$, which can deviate
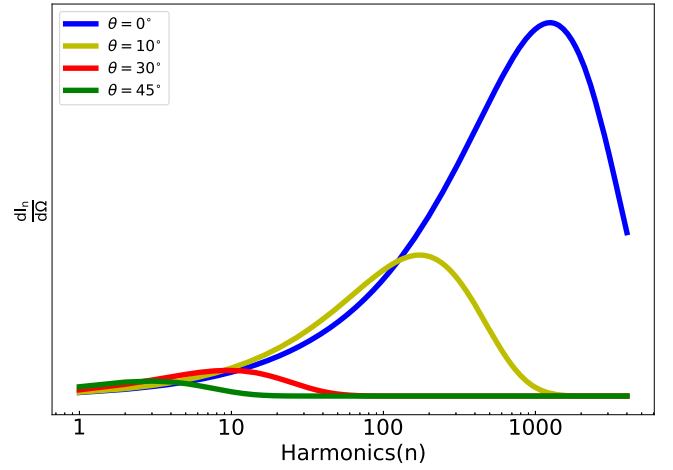

Figure 1. For $B = 5 \times 10^{11}$ G and $\gamma = 10$, the synchrotron spectra are shown as functions of the multipoles (Equation (1)) for different latitudes. The figure shows the role of high-latitude emission in introducing spectral curvature.

significantly from unity for large angles even for $\beta \simeq 1$. We find that it is possible to approximate the Bessel function and its derivative in Equation (1) using the stationary phase approximation even when β' deviates significantly from unity (Schwinger et al. 1998 employs this method in the angle-averaged case for $\beta \simeq 1$). This allows us to obtain the following approximate expressions for the Bessel function and its derivative (see Appendix for details):

$$J_n(n\beta') \simeq 0.447n^{-1/3}\beta'^{-1/3} \text{ for } n \leqslant n_c$$
$$J_n(n\beta') \simeq 0.335n^{-1/2}(1 - \beta')^{-1/4}\beta'^{-1/4}$$
$$\times \exp\left(-2\frac{\sqrt{2}}{3}n\beta'^{-1/2}(1 - \beta')^{3/2}\right) \text{ for } n \geqslant n_c$$
$$J_n'(n\beta') \simeq 0.411n^{-2/3}\beta'^{-2/3} \text{ for } n \leqslant n_c$$
$$J_n'(n\beta') \simeq 0.474n^{-1/2}(1 - \beta')^{1/4}\beta'^{-3/4}$$
$$\times \exp\left(-2\frac{\sqrt{2}}{3}n\beta'^{-1/2}(1 - \beta')^{3/2}\right) \text{ for } n \geqslant n_c,$$
$$(2)$$

with

$$n_c \simeq \frac{\beta'^{1/2}}{(1 - \beta')^{3/2}}. \quad (3)$$

n_c denotes the harmonic at which spectral cutoff occurs. The analytic expressions given in Equation (2) agree with the numerical results to better than 10% in the acceptable range of $\beta' \gtrsim 0.3$. Also, for $\beta' \simeq 1$ ($\beta \simeq 1$ and $\theta \simeq 0$), $1/(1 - \beta') \simeq 2\gamma^2$ and $n_c \simeq \gamma^3$, which agrees with the angle-averaged case (Schwinger et al. 1998).

Our aim in this paper is to explain the spectral cutoff as observed in ULXs. For fitting the X-ray continuum spectral data, we require $n_c \gg 1$, which constrains the latitude $\theta \lesssim 70°$. One can consider the intriguing possibility that the observed spectrum could arise from a set of discrete lines (though it is unlikely, as we argue below). This requires: $n_c \gtrsim 1$, which gives $0.3 \lesssim \beta \lesssim 1$ and $0.3 \lesssim \cos\theta \lesssim 1$.[1] We note that the exponential terms in Equation (2) adequately capture the cutoff

---

[1] https://www.wolfram.com/mathematica/

frequency in the entire parameter range of interest, which is key to modeling the ULX cutoff frequency. While we compute the Bessel functions numerically for data analysis, these analytic expressions help us interpret our results.

In Figure 1, we display synchrotron spectra for emission from different latitudes. Equation (2) allows us to understand the spectral shapes seen in the figure. The spectral cutoff occurs at an angular frequency $\omega \simeq n_c \omega_B$. For emission close to the plane of the rotation ($\theta \simeq 0$), $n_c \simeq \gamma^3$. However, for larger angles $n_c < \gamma^3$, as Equation (2) shows, and the spectral cutoff shifts to smaller frequencies. As we discuss later, the spectral cutoff in the data we analyze occurs at $E \simeq 10$ keV, which is possible for a range of γ, B, and θ as will be discussed below in more detail. Even though we only assume electron motion in the plane perpendicular to the magnetic field, our results do not qualitatively change if the electron has a z-component of velocity. This case can be incorporated into our analysis by altering B to $B_\perp \equiv B \cos \chi$, where χ is the angle between the velocity vector and the magnetic field (e.g., Landau & Lifshitz 1975).

3. Data

We utilize the NuSTAR observations of two bright pulsar ULXs, NGC 5907 ULX1 (R.A.: 15 15 58.62, decl.: +56 18 10.3; Israel et al. 2017a; Walton et al. 2015; Fürst et al. 2017) and NGC 7793 P13 (R.A.: 23 57 50.9, decl.: −32 37 26.6; Fürst et al. 2016; Israel et al. 2017b; Walton et al. 2018b), to compare our theoretical model against data. The distances to the host galaxies are $\simeq 17.1$ Mpc (e.g., Fürst et al. 2017) and $\simeq 3.5$ Mpc (e.g., Walton et al. 2018b), respectively. These two sources were observed by NuSTAR several times in the past decade, which provides us with an opportunity to verify the consistency of the theory over the long-term spectral evolution of the sources. In particular, for NGC 7793 P13, we detect two distinct flux states. The choice of the instrument is motivated by its energy coverage, which allows us to model the spectral curvature of the source. The broadband spectra of ULXs are generally fitted with multiple components: neutral absorption, accretion disk (geometrically thin or slim), and a phenomenological model of either magnetic or nonmagnetic Comptonization processes (see, e.g., Kaaret et al. 2017). The thermal disk component and neutral absorption mostly play a role in the soft energy regime ($E \lesssim 5$ keV). Our aim in this paper is to explain the spectral cutoff in ULXs, which occurs in a higher energy range ($E \simeq 10$ keV). To minimize contamination from soft components and to adequately model the spectral break, we study the energy range $\simeq 5$–25 keV in this paper. In our study, we consider all the available NuSTAR data sets for both sources. However, for NGC 5907 ULX1, there are a few observations for which the signal-to-noise ratio is poor owing to the faintness of the source. We do not utilize these data for our analysis.

3.1. Data Reduction Process

The NuSTAR data are extracted using the HEASOFT version 6.29.[2] We use the nupipeline tool to extract cleaned products and the nuproducts tool to extract the source and background spectra and the response files from both the FPMA and FPMB modules. In general we follow the method outlined in previous works (e.g., Walton et al. 2015, 2018b; Fürst et al. 2017, 2016; Israel et al. 2017a, 2017b; Lin et al. 2022) for data reduction of these two sources. We choose the source photon extraction region as 50″ radius circle for both sources. The background regions are selected as 100″ radius circle in all the cases. The number of counts per energy bin for grouping the spectra are a minimum of 30 counts per energy bin for all NGC 5907 ULX1 spectra and 50 counts per bin for NGC 7793 P13 spectra where the source is in a high-flux state, and 20 counts per energy bin for a low-flux state (observation IDs 30502019002, 30502019004, 50401003002, 90601327002) of the source.

After we obtain the spectra, we use the XSPEC (Arnaud 1996) spectral analysis package to convert the spectra into flux units for further analysis. NuSTAR spectra beyond $\simeq 25$ keV are dominated by the background for both the sources, and therefore spectral data above this energy are not utilized in our analysis. In some low-flux-state observations, the background starts dominating well below $\simeq 20$ keV; however, to provide similar treatment to all observations, we take spectra up to $\simeq 25$ keV for all cases. We fit the NuSTAR spectra with a cutoff power-law model (in XSPEC the syntax is constant*cutoffpl). The constant model represents the instrumental cross-calibration differences, and cutoffpl is the continuum representing an exponentially cutoff power-law spectrum. This model for 5.0–25.0 keV spectra give statistically good fit for both the sources. For the cutoffpl model, we fix the index to 0.59, a typical value for ULX pulsars (see, e.g., Walton et al. 2020). We do not consider neutral absorption, as it plays a role only in the softer regime of the spectra. We then convert the spectral counts into flux νF_ν (erg cm^{-2} s^{-1}) by the eeufspec command and take the data points in the energy range 5.0–25.0 keV ($\simeq 1.2$–6.0×10^{18} Hz) to perform further analysis, as described in the Section 4. We have further verified the robustness of this data extraction procedure with another model, such as a simple powerlaw of photon index 0, instead of the cutoffpl model, and extract the spectra in flux unit using eeufspec. We find that our results are insensitive to the choice of XSPEC models used to generate the flux data points.

4. Analysis and Results

From Equation (1), one can verify that γ and B are degenerate with each other if $\beta \simeq 1$. As we wish to explore a range of electron speeds from semirelativistic to ultrarelativistic, this degeneracy cannot be removed.[3] Thus we choose γ_{min}/B as one of the parameters in the analysis. We use three parameters—γ_{min}/B, θ, and N—in our analysis and later fix one more parameter to deal with residual degeneracies. We also convert the model to νF_ν unit by appropriately scaling Equation (1) by a multiplicative factor $n = \omega/\omega_B$, where $\omega = 2\pi\nu$.

For our model, the observed flux can be written as:

$$\nu F_\nu = N' \int_{x_{min}}^{x_{max}} S x^{-p} \exp(-x/x_{max}) \, dx, \qquad (4)$$
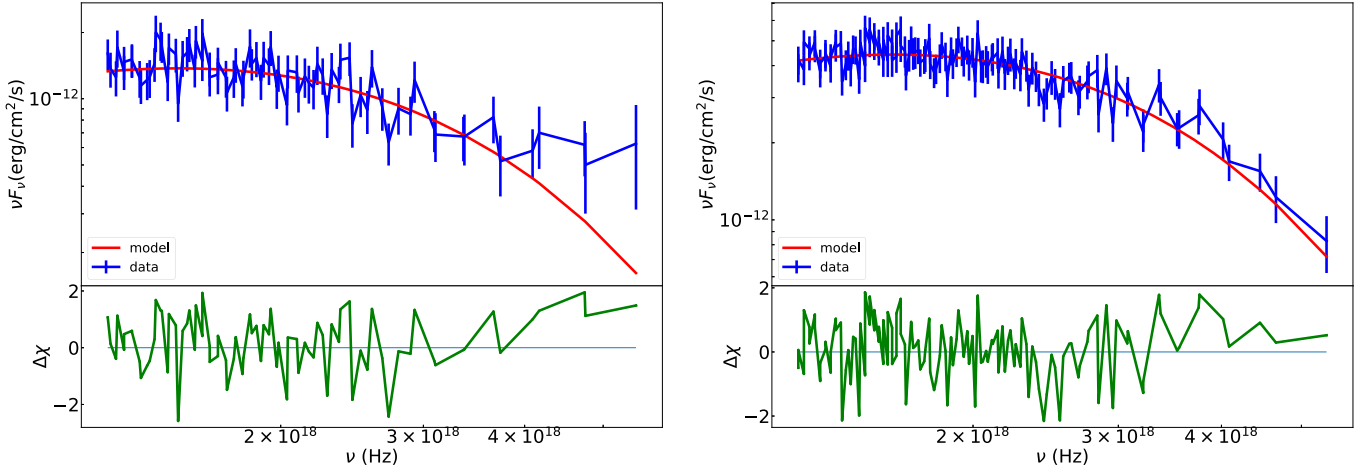
Figure 2. Example plot showing spectral fitting of the theoretical model on one observation for each source. The top panels show the data with the model overplotted, and the corresponding residuals are shown in the bottom panels. The models shown here are for a 1° angle in the case of NGC 5907 ULX1 (left; Observation 80001042002) and a 30° angle for NGC 7793 P13 (right; Observation 90301326002).

Table 1
Best-fit Parameters and χ^2 from Python Curve Fit for Seven NuSTAR Observations of NGC 5907 ULX1 and 10 NuSTAR Observations of NGC 7793 P13 Are Listed

Observations	$\theta = 1°$			$\theta = 15°$			$\theta = 30°$		
	$x_{\min}$ $(10^{-7}\,\mathrm{G}^{-1})$	N $(10^{-17}\,\mathrm{cm}^{-2})$	χ^2/d.o.f	$x_{\min}$ $(10^{-10}\,\mathrm{G}^{-1})$	N $(10^{-18}\,\mathrm{cm}^{-2})$	χ^2/d.o.f	$x_{\min}$ $(10^{-11}\,\mathrm{G}^{-1})$	N $(10^{-19}\,\mathrm{cm}^{-2})$	χ^2/d.o.f
NGC 5907 ULX1									
30002039005	(9.54 ± 0.56)	(1.10 ± 0.18)	57/49	(2.81 ± 0.16)	(0.70 ± 0.12)	57/49	(3.45 ± 0.20)	(2.97 ± 0.49)	57/49
30302004006	(6.38 ± 0.36)	(1.00 ± 0.12)	66/52	(1.88 ± 0.11)	(0.63 ± 0.08)	66/52	(2.31 ± 0.13)	(2.72 ± 0.34)	66/52
30302004008	(5.94 ± 0.35)	(0.81 ± 0.10)	62/49	(1.75 ± 0.10)	(0.51 ± 0.06)	62/49	(2.15 ± 0.12)	(2.21 ± 0.27)	62/49
80001042002	(7.69 ± 0.27)	(2.52 ± 0.23)	80/78	(2.27 ± 0.08)	(1.60 ± 0.14)	80/78	(2.78 ± 0.10)	(6.84 ± 0.61)	80/78
80001042004	(6.57 ± 0.26)	(1.69 ± 0.15)	82/77	(1.94 ± 0.08)	(1.07 ± 0.10)	82/77	(2.38 ± 0.09)	(4.58 ± 0.41)	83/77
90501331002	(5.97 ± 0.46)	(0.47 ± 0.08)	34/39	(1.76 ± 0.14)	(0.30 ± 0.05)	34/39	(2.16 ± 0.16)	(1.28 ± 0.21)	34/39
90601323002	(7.23 ± 0.29)	(1.66 ± 0.16)	89/88	(2.13 ± 0.09)	(1.05 ± 0.10)	90/88	(2.62 ± 0.10)	(4.50 ± 0.43)	90/88
NGC 7793 P13									
30302005002	(7.66 ± 0.20)	(3.07 ± 0.20)	77/82	(2.26 ± 0.06)	(1.95 ± 0.13)	77/82	(2.77 ± 0.07)	(8.30 ± 0.55)	77/82
30302005004	(7.46 ± 0.15)	(4.58 ± 0.23)	111/117	(2.20 ± 0.04)	(2.90 ± 0.15)	111/117	(2.70 ± 0.05)	(12.40 ± 0.62)	111/117
30302015002	(7.53 ± 0.14)	(5.95 ± 0.27)	147/133	(2.22 ± 0.04)	(3.77 ± 0.17)	147/133	(2.73 ± 0.05)	(16.10 ± 0.73)	148/133
30302015004	(7.53 ± 0.17)	(4.75 ± 0.26)	130/123	(2.22 ± 0.05)	(3.02 ± 0.17)	130/123	(2.72 ± 0.06)	(12.88 ± 0.70)	130/123
30502019002	(7.41 ± 0.53)	(0.65 ± 0.11)	42/61	(2.18 ± 0.16)	(0.41 ± 0.07)	42/61	(2.68 ± 0.19)	(1.77 ± 0.30)	42/61
30502019004	(6.93 ± 0.62)	(0.57 ± 0.12)	32/42	(2.04 ± 0.18)	(0.36 ± 0.08)	32/42	(2.51 ± 0.22)	(1.55 ± 0.32)	32/42
50401003002	(7.37 ± 0.79)	(0.59 ± 0.15)	25/31	(2.17 ± 0.23)	(0.38 ± 0.10)	25/31	(2.67 ± 0.28)	(1.60 ± 0.41)	25/31
80201010002	(7.26 ± 0.10)	(6.20 ± 0.22)	156/204	(2.14 ± 0.03)	(3.94 ± 0.14)	156/204	(2.63 ± 0.04)	(16.81 ± 0.58)	156/204
90301326002	(7.20 ± 0.14)	(7.11 ± 0.33)	104/123	(2.12 ± 0.04)	(4.51 ± 0.21)	104/123	(2.61 ± 0.05)	(19.26 ± 0.89)	105/123
90601327002	(9.65 ± 1.01)	(1.00 ± 0.30)	35/34	(2.84 ± 0.30)	(0.63 ± 0.19)	35/34	(3.49 ± 0.36)	(2.70 ± 0.80)	35/34

Note. The errors are calculated for a 1σ confidence from the covariance matrix using the parameter `absoulte_sigma = True`.

where $x = \gamma/B$,

$$N' = \frac{N}{\int_{x_{\min}}^{x_{\max}} x^{-p} \exp(-x/x_{\max})\,dx}, \quad (5)$$

and

$$S = \frac{2\pi e^2 \nu^3}{c\nu_B}\left[\tan^2\theta J^2_{\frac{\nu}{\nu_B}}\left(\frac{\nu}{\nu_B}\cos\theta\right) + J'^2_{\frac{\nu}{\nu_B}}\left(\frac{\nu}{\nu_B}\cos\theta\right)\right]. \quad (6)$$

To explore the congruence of the data and the model, we choose two different statistical methods–frequentist approach and Bayesian analysis. Given that it is hard to determine the best fit and the errors on the three parameters simultaneously,

we fix the angle θ and keep the other two parameters $\gamma_{\min}/B = x_{\min}$ and N free to vary. For the frequentist approach, we first carry out a minimum χ^2 analysis using the `scipy` (Virtanen et al. 2020) "curve_fit" tool.[4] The best-fit parameters, χ^2 values, and 1σ errors (computed using covariance matrix) are given in Table 1. For each data set, we consider three values of $\theta = 1°$, 15°, 30° for our analysis. As discussed in the foregoing, this choice is based on the acceptable range of latitudes to ensure $n_c \gg 1$. In Figure 2 we plot the data, the

---

[4] https://docs.scipy.org/doc/scipy/reference/generated/scipy.optimize.curve_fit.html

best-fit curve, and the spectral residuals for one observation for each source.

In the Bayesian analysis, we utilize the Markov Chain Monte Carlo (MCMC) method using the `python emcee` package[5] (Foreman-Mackey et al. 2013). We find convergence in each case, and the computed posterior probabilities agree with the results obtained using the frequentist method.

We next discuss the physical implications of the parameter range suggested by statistical analyses. We find that for fixed emission angles, the spectrum is scaled by parameter x_{min}, and the overall amplitude is scaled by N. For both sources, we do not find significant long-term spectral variability in the high-energy band as the parameter x_{min} remains nearly the same for all observations (Table 1). However, due to flux changes in different epochs of observation, parameter N varies significantly.

For the range of θ shown in Table 1, the estimated range of $x_{min} = \gamma_{min}/B$ varies from 10^{-6} to 10^{-11} G^{-1}. It can be verified from the expression for $\nu_B = \omega_B/(2\pi)$ and Equation (3) that the results given in Table 1 correspond to a cutoff frequency of around 10 keV. The allowed range of x_{min} encompasses a large range of particle speeds and magnetic field strengths. At higher latitudes, our results are consistent with semirelativistic electrons, $\gamma_{min} \simeq 20$ and $B \simeq 10^{12}$ G. This magnetic field strength is expected on the surface of neutron stars (e.g., Caballero & Wilms 2012; Pétri 2016). The overall normalization $N = \rho_N V/D^2$ is highly uncertain as both the relativistic electron density ρ_N and the volume of emission region V are very poorly determined even theoretically. Typically, in neutron star magnetosphere, the lower limit of the plasma density is given by the Goldreich–Julian limit (Goldreich & Julian 1969), which depends on the pulsar spin period, magnetic field strength, and alignment of the spinning axis with the magnetic field lines. Depending on the volume of the emission region, we find that the estimated number density could be comparable to or higher than the Goldreich–Julian limit (Goldreich & Julian 1969) for a 1 s spinning pulsar with $B \simeq 10^{12}$ G, i.e., 7×10^{10} particles cm^{-3}. In reality, the plasma density can be significantly higher than the Goldreich–Julian limit (see Lyutikov & Gavriil 2006 and references therein). This means our results are consistent with this theoretical expectation. We also determine that, for a range of acceptable parameters, the emitting region is optically thin to synchrotron self-absorption and Compton scattering.

If we restrict the maximum limit of the magnetic field on the NS surface to the Schwinger limit of 4.4×10^{13} G, the magnetic field strength at which the quantum effects become important, then the maximum value of γ_{min} can be estimated. For lower x_{min} (i.e., lower γ_{min} or higher B), we get emission at higher latitudes, which requires a lower value of N to explain the observed ULX flux. On the other hand, when x_{min} is higher, we get emission closer to the plane of orbit and higher N is required to generate such high flux in these sources. It would be possible in the future to constrain all the parameters adequately if we can have at least one parameter determined from other data. Our results point to the possibility that the spectral curvature in ULXs might have a common origin and all ULXs are possibly highly magnetized neutron stars. This theoretical model can also be employed to explain the high-energy cutoff in X-ray binary pulsar sources. Essentially, this model suggests

---

that the curvature in the spectrum is governed by the plasma velocity, magnetic field strength, electron number density, and emission angle.

5. Discussion

In this paper, we seek to explain the X-ray spectra of two known pulsar ULXs. In particular, we focus on the cutoff in such spectra at $E \simeq 10$ keV, which is a generic feature of many pulsar ULXs. We propose synchrotron radiation at a range of latitudes as the possible physical process to explain this observed spectral shape. Our main results, based on the analysis of 17 spectra of the two sources, are summarized in Table 1. Figure 2 shows the fit and its residual for one spectrum for each source.

Other models that have been explored to explain the dominant emission in the hard X-ray range in ULXs invoke Comptonization from the coronal region of nonmagnetic sources and Comptonization from the magnetized column in neutron stars (see, e.g., West et al. 2018; Walton et al. 2020). Compton scattering in the presence of high magnetic fields in neutron stars is a possible candidate to explain the high luminosity in these sources (Mushtukov et al. 2015). In principle, there could be two possible ways to distinguish our proposed scenario from these models.

Table 1 shows the best-fit value $x_{min} = \gamma_{min}/B \simeq 2 \times 10^{-11}$ G^{-1} for $\theta \simeq 30°$. This could correspond, for instance, to a semirelativistic electron ($\gamma_{min} \simeq 20$) along with a magnetic field $B \simeq 10^{12}$ G. In such cases, the fundamental mode of emission is $\nu_B = eB/(2\pi m_e c \gamma_{min}) \simeq 600$ eV. As this is larger than the spectral resolution of NuSTAR in the energy range of interest, the observed spectrum could be a set of discrete cyclotron lines. In practice, such an interpretation could be difficult owing to mixing with larger γ values and the width of spectral lines, which are difficult to ascertain. This would also require either reanalysis of the data or new data, which is beyond the scope of the paper. Our analysis raises the intriguing possibility that the discreteness of the spectrum could probe the latitude of the emission. As we have already discussed in Section 2, an upper limit on the latitude of emission can be obtained by requiring $n_c \gg 1$; this yields a stringent upper bound $\theta \simeq 70°$. For fitting continuum X-ray spectral data in the energy range of interest, this requirement motivates the upper limit of $\theta \simeq 30°$ that we use in this paper.

Another possible probe of our model could be the polarization of the received photons. Photons emerging from higher latitudes would be elliptically polarized while those closer to the plane of the orbit would be linearly polarized. While nonmagnetic Comptonization will not show polarized emission, magnetic Comptonization and synchrotron radiation could display different degrees of polarization. Modern X-ray polarimeters such as the Imaging X-ray Polarimetry Explorer (Weisskopf et al. 2016) and the upcoming X-ray Polarimeter Satellite (XPoSat) mission with the X-ray polarimeter instrument POLIX (Paul 2022) might be able to address these questions.

We provide a brief summary of our main results and perspectives below:

1. We propose that the spectral cutoff in ULXs arises from classical, high-latitude, and optically thin synchrotron radiation. For classical radiation, the cutoff occurs at energies $\gamma^3 \nu_B$ for radiation close to the plane of the orbit,

but the cutoff frequency shifts to much smaller frequencies for high-latitude emission. Quantum effects only dominate the cutoff for energies close to the electron rest mass and hence cannot be responsible for the observed cutoff at $E \simeq 10$ keV.

2. This model is compared with 17 spectra, corresponding to different flux states of two ULXs. The observed fluxes are modeled using four theoretical parameters. Given the degeneracy between these parameters, only two parameters can be estimated from the data. To test the robustness of our statistical analysis, we carry out both frequentist and Bayesian analysis (using MCMC). While our analysis yields a large range of possible theoretical models, the most interesting case corresponds to high-latitude emission ($\theta \simeq 30°$) from a semirelativistic plasma from the surface of the neutron star ($B \simeq 10^{12}$ G and $\gamma \simeq 20$). The statistical analysis also allows us to establish that the plasma is optically thin for a plausible range of parameters.

3. It is possible to verify the model using X-ray polarization data, which might be available in the near future. Another possible probe of the semirelativistic plasma could be the discreteness of the observed spectrum, which we have briefly discussed.

Appendix
Analytic Approximation of the Bessel Function

The starting point of approximating the Bessel function and its derivatives is the integral representation of these functions (e.g., Landau & Lifshitz 1975; Schwinger et al. 1998),

$$J_n(z) = \int_0^\pi d\phi \frac{1}{\pi} \cos(z \sin\phi - n\phi), \qquad (A1)$$

$$J_n'(z) = -\int_0^\pi d\phi \frac{1}{\pi} \sin\phi \sin(z \sin\phi - n\phi). \qquad (A2)$$

Here $z = n\beta \cos\theta = n\beta'$. As the integrands are highly oscillatory, the main contribution to the integrals arises from regions near $\phi = 0$ when the phase is large (stationary phase approximation). This is ensured by the condition $n\beta' \gg 1$.

Expanding the phase of $J_n(z)$ around $\phi = 0$, we get:

$$z \sin\phi - n\phi = n\beta' \sin\phi - n\phi = -n\left[\phi(1 - \beta') + \frac{\beta'\phi^3}{3!}\right].$$
(A3)

Making the substitution, $\phi = (1 - \beta')^{1/2} x / \beta'^{1/2}$ yields:

$$\phi(1 - \beta') + \frac{\beta'\phi^3}{3!} = \frac{(1 - \beta')^{3/2}}{\beta'^{1/2}}\left(x + \frac{x^3}{6}\right). \qquad (A4)$$

In this case, the stationary phase points are located at:

$$x = \pm\sqrt{2}\,i. \qquad (A5)$$

Following the procedure outlined in Schwinger et al. (1998), in the neighborhood of the stationary phase point, we can write:

$$x = \sqrt{2}\,i + \xi, \qquad (A6)$$

where ξ is real and small, which gives:

$$x + \frac{x^3}{6} = \sqrt{2}\,i\left(\frac{2}{3} + \frac{\xi^2}{2}\right). \qquad (A7)$$

This allows us to write:

$$J_n(n\beta') = \int_0^\infty dx \frac{1}{\pi} \frac{(1 - \beta')^{1/2}}{\beta'^{1/2}}$$
$$\times \cos\left(n\left[\frac{(1 - \beta')^{3/2}}{\beta'^{1/2}}\left(x + \frac{x^3}{6}\right)\right]\right). \qquad (A8)$$

First, we deal with the case when $n(1 - \beta')^{3/2}/\beta'^{1/2} \ll 1$. In this case, the main contribution to the integral comes from the region where x is large. Given that most of the contribution to the integral comes from regions where the phase is close to unity, the integration limit can be extended to infinity (e.g., Schwinger et al. 1998). Solving the resultant integral, we get:

$$J_n(n\beta') \simeq 0.447 n^{-1/3} \beta'^{-1/3} \text{ for } n\frac{(1 - \beta')^{3/2}}{\beta'^{1/2}} \ll 1. \quad (A9)$$

For $n(1 - \beta')^{3/2}/\beta'^{1/2} \gg 1$, the integral can be written as:

$$J_n(n\beta') = \text{Re} \int_0^\infty dx \frac{1}{\pi} \frac{(1 - \beta')^{1/2}}{\beta'^{1/2}}$$
$$\times \exp\left(in(1 - \beta')^{3/2}(x + x^3/6)/\beta'^{1/2}\right). \quad (A10)$$

This can readily be integrated as most of the contribution arises from regions close to $x \simeq 0$:

$$J_n(n\beta') \simeq 0.335 n^{-1/2}(1 - \beta')^{-1/4}\beta'^{-1/4}$$
$$\times \exp\left(-2\frac{\sqrt{2}}{3}n\beta'^{-1/2}(1 - \beta')^{3/2}\right). \qquad (A11)$$

Following a similar calculation procedure, we obtain the approximate forms of $J_n'(n\beta')$ in Equation (2).

Our analysis extends the procedure outlined by Schwinger et al. (1998) for the extreme relativistic case $\beta' \simeq 1$ to arbitrary β'. We note that the analytic expressions we derive yield excellent fits to numerical results for $\beta' \gtrsim 0.3$.

ORCID iDs

Tanuman Ghosh ⓘ https://orcid.org/0000-0002-3033-5843

References

Allen, G. E., Petre, R., & Gotthelf, E. V. 2001, ApJ, 558, 739
Arnaud, K. A. 1996, in ASP Conf. Ser. 101, Astronomical Data Analysis Software and Systems V, ed. G. H. Jacoby & J. Barnes (San Francisco, CA: ASP), 17
Bachetti, M., Harrison, F. A., Walton, D. J., et al. 2014, Natur, 514, 202
Bachetti, M., Rana, V., Walton, D. J., et al. 2013, ApJ, 778, 163
Caballero, I., & Wilms, J. 2012, MmSAI, 83, 230
Foreman-Mackey, D., Hogg, D. W., Lang, D., & Goodman, J. 2013, PASP, 125, 306
Fürst, F., Walton, D. J., Harrison, F. A., et al. 2016, ApJL, 831, L14
Fürst, F., Walton, D. J., Stern, D., et al. 2017, ApJ, 834, 77
Goldreich, P., & Julian, W. H. 1969, ApJ, 157, 869
Harrison, F. A., Craig, W. W., Christensen, F. E., et al. 2013, ApJ, 770, 103
Heinz, S. 2004, MNRAS, 355, 835
Israel, G. L., Belfiore, A., Stella, L., et al. 2017a, Sci, 355, 817
Israel, G. L., Papitto, A., Esposito, P., et al. 2017b, MNRAS, 466, L48
Kaaret, P., Feng, H., & Roberts, T. P. 2017, ARA&A, 55, 303
King, A., & Lasota, J.-P. 2016, MNRAS, 458, L10
King, A., & Lasota, J.-P. 2020, MNRAS, 494, 3611
King, A., Lasota, J.-P., & Kluźniak, W. 2017, MNRAS, 468, L59
Kisaka, S., & Tanaka, S. J. 2017a, ApJ, 837, 76
Kisaka, S., & Tanaka, S. J. 2017b, JPhCS, 932, 012015
Landau, L. D., & Lifshitz, E. M. 1975, The Classical Theory of Fields (Oxford: Pergamon)
Lin, L. C.-C., Hu, C.-P., Takata, J., et al. 2022, ApJ, 924, 65
Longair, M. S. 2011, High Energy Astrophysics (Cambridge: Cambridge University Press)
Lyutikov, M., & Gavriil, F. P. 2006, MNRAS, 368, 690
Maccarone, T. J. 2005, MNRAS, 360, L68
Markoff, S., Nowak, M. A., & Wilms, J. 2005, ApJ, 635, 1203
Mushtukov, A. A., Ingram, A., Middleton, M., Nagirner, D. I., & van der Klis, M. 2019, MNRAS, 484, 687
Mushtukov, A. A., Suleimanov, V. F., Tsygankov, S. S., & Ingram, A. 2017, MNRAS, 467, 1202
Mushtukov, A. A., Suleimanov, V. F., Tsygankov, S. S., & Poutanen, J. 2015, MNRAS, 454, 2539
Mushtukov, A. A., Tsygankov, S. S., Suleimanov, V. F., & Poutanen, J. 2018, MNRAS, 476, 2867
Nasa High Energy Astrophysics Science Archive Research Center (Heasarc) 2014, HEAsoft: Unified Release of FTOOLS and XANADU, Astrophysics Source Code Library, ascl:1408.004
Paul, B. 2022, 44th COSPAR Scientific Assembly, E1.12–0010–22
Pétri, J. 2016, JPlPh, 82, 635820502
Reynolds, S. P., & Keohane, J. W. 1999, ApJ, 525, 368
Riegler, G. R. 1970, Natur, 226, 1041
Rybicki, G. B., & Lightman, A. P. 1979, Radiative Processes in Astrophysics (New York: Wiley)
Schwinger, J., DeRaad, L. L., Milton, K., & Tsai, W.-Y. 1998, Classical Electrodynamics (1st ed.; Boca Raton, FL: CRC Press)
Virtanen, P., Gommers, R., Oliphant, T. E., et al. 2020, NatMe, 17, 261
Walton, D. J., Fuerst, F., Harrison, F., et al. 2013, ApJ, 779, 148
Walton, D. J., Fürst, F., Harrison, F. A., et al. 2018b, MNRAS, 473, 4360
Walton, D. J., Fürst, F., Heida, M., et al. 2018a, ApJ, 856, 128
Walton, D. J., Harrison, F. A., Bachetti, M., et al. 2015, ApJ, 799, 122
Walton, D. J., Pinto, C., Nowak, M., et al. 2020, MNRAS, 494, 6012
Weisskopf, M. C., Ramsey, B., O'Dell, S., et al. 2016, Proc. SPIE, 9905, 990517
West, L. A., Lehmer, B. D., Wik, D., et al. 2018, ApJ, 869, 111